scientific reports

Check for updates

OPEN

Sol–gel synthesized calcium borate glass and glass–ceramics: effect of $CrCl_3$ doping on structure, mechanics, and gamma-ray shielding efficiency

Norah Alsairy[1], M. A. Madshal[2]✉ & Ashrf Althbiti[3]

This study presents the synthesis and characterization of chromium chloride-doped calcium borate glasses and glass ceramics. Samples with the nominal composition 55CaO-(45-*x*)B_2O_3-*x*$CrCl_3$ (where *x* = 0, 1, 2, and 3 mol%) were successfully prepared via the sol-gel method. X-ray diffraction (XRD) analysis confirmed that the specimens retained an amorphous nature following calcined at 500 °C for 4 h. However, a distinct transition to a glass-ceramic phase was observed upon increasing the temperature to 700 °C. Morphological characteristics were analyzed using field emission scanning electron microscopy (FESEM). FTIR spectroscopy revealed a progressive increase in the fraction of tetrahedral units (BO_4), rising from 43 to 46% with increasing $CrCl_3$ content, which increased the rigidity of the prepared glass samples. The radiation shielding efficiency was computationally evaluated using the Phy-X/PSD online software. The results demonstrated that $CrCl_3$ integration effectively reduced the half-value layer (HVL), the tenth-value layer (TVL), and the mean free path (MFP). At 0.04 MeV, the HVL, TVL, and MFP values decreased from 0.336 cm, 1.115 cm and 0.484 cm for the 0CrCaB to 0.252 cm, 0.839 cm, and 0.364 cm for the 3CrCaB sample, respectively. In contrast, the mass attenuation coefficient increased from 0.803 cm^2/g for the 0CrCaB to 0.883 cm^2/g for the 3CrCaB sample. Furthermore, the mechanical properties were theoretically calculated using the Makishima–Mackenzie model. Young's modulus (*Y*) increased from 66.137 to 108.00 GPa, bulk modulus (*B*) increased from 47.619 to 90.720 GPa, shear modulus (*S*) increased from 26.069 to 41.488 GPa, and microhardness (*H*) increased from 4.023 to 5.4878 GPa. The density progressively increased from 2.57 to 3.11 g/cm^3 with rising $CrCl_3$ content, while the molar volume simultaneously decreased from 24.19 cm^3/mol to 20.85 cm^3/mol. These findings suggest that the synthesized samples can potentially be used as radiation shields.

Keywords Mechanical properties, Radiation shielding properties, FTIR analysis, Oxychloride glasses and glass ceramics

Borate glasses and glass ceramics have attracted increased attention due to their unique properties, making them suitable for a wide range of applications[1]. Key advantages of borate glasses include their excellent linear optical response, superior mechanical qualities, energy dependence, high thermal and chemical stability, and high sensitivity for low-dose radiation measurements[2]. Compared to silica glasses, borate glasses have lower melting and softening temperatures[3]. For instance, pure borate glass has a melting temperature of approximately 450 °C, while pure silicate glass melts at around 1728 °C[4]. However, pure B_2O_3 glass has limited practical use due to its poor chemical durability and high affinity for water[5]. To overcome these drawbacks, various oxides, such as CaO, SrO, and SiO_2, are incorporated into the B_2O_3 network to enhance chemical durability[6]. Binary calcium borate glasses have received considerable attention from various borate systems due to their exceptional properties, including remarkable bioactivity and shielding applications[7,8]. Additionally, incorporating CaO enhances the

[1]Department of Physics, College of Turabah, Taif University, P.O. BOX 11099, 21944 Taif, Saudi Arabia. [2]Physics Department, Faculty of Education, Humanity & Applied Science, Sana'a University, Khawlan, Sana'a, Yemen. [3]Department of Information Technology, College of Computers and Information Technology, Taif University, 21944 Taif, Saudi Arabia. ✉email: m.a.madshal@su.edu.ye

mechanical strength, chemical durability, and thermal stability of borate glass, making it more suitable for real-world applications[9]. Nowadays, ionizing radiation is used worldwide across various fields, including medical and dental facilities and environmental protection. Given that shielding performance depends on the specific energy and type of radiation, different materials have been proposed to ensure adequate protection[10]. For this reason, many researchers have recently focused on developing new shielding materials to mitigate radiation leakage and its harmful consequences[11–13]. These efforts aim to protect living tissues and cells from radiation-induced damage, safeguard sensitive technologies, and reduce negative environmental impacts. Among the materials under investigation are glass, polymers, and various composite materials, each offering unique properties that make them suitable for radiation shielding applications[14,15]. Glass, in particular, stands out due to its relatively low cost, ease of fabrication, and versatility. It can be molded into different shapes and thicknesses, making it adaptable to a range of shielding needs. Furthermore, recent research has focused on the development of glass and glass-ceramic composites incorporated with heavy metals to achieve high-performance radiation shielding, thereby broadening their utility in medical and nuclear fields[1,16]. Borate, silicate, and borosilicate glasses doped with transition-metal oxides have also attracted interest due to their appealing combination of physical and chemical properties[17–19]. For example, J. Sumalatha M et al.[17] reported that the incorporation of chromium ions into the borosilicate glass network has demonstrated an improvement in gamma-ray attenuation ability due to the higher atomic number and density of Cr ions, which enhance photon interaction probabilities. In a glass matrix, Cr ions can exist in three oxidation states: Cr^{3+}, Cr^{5+}, and Cr^{6+}. Cr^{3+} ions act as a glass modifier with CrO_6 structural units, while Cr^{5+} and Cr^{6+} ions act as glass formers[20]. The incorporation of chromium ions into the glass network significantly alters the material's structure and properties, particularly in the formation of glass ceramics[21]. They can enhance the material's compactness and density, reducing porosity and improving the mechanical strength, which is crucial for radiation shielding applications. Increased density enhances the material's ability to attenuate radiation, especially high-energy photons such as gamma rays. The crystalline phases introduced by Cr ions not only increase mechanical strength and thermal stability but also enhance overall shielding efficiency by creating a more ordered, tightly packed structure that better absorbs and scatters incoming radiation[22]. The radiation shielding performance of glass and glass ceramics depends on their composition. Therefore, selecting the appropriate glass formulation is critical to achieving optimal radiation attenuation. It is also known that chloride tends to volatilize during melting. However, in the preparation of glass materials, some studies have explored chloride-containing glasses[23,24]. For example, Xiaojing Chen et al.[24] synthesized calcium metasilicate glass using a high concentration of calcium chloride in place of calcium oxide. Their findings showed that the glass retained chloride, which influenced its physical properties, indicating structural changes in the glass network due to chloride incorporation. The development of high-performance radiation shielding materials remains a critical priority in nuclear safety, medical diagnostics, and radiation protection technologies. In recent years, glass and glass-ceramic systems have attracted considerable attention as potential matrices for radiation shielding applications due to their compositional flexibility, chemical stability, and tunable physical properties[25,26]. Among these systems, calcium borate glasses have emerged as promising candidates owing to their favorable structural characteristics and good glass-forming ability. Previous studies have extensively investigated oxide and oxyfluoride glass systems for radiation shielding applications, demonstrating significant improvements in attenuation performance through compositional modification[8,10,11]. However, from the best of our knowledge, studies on oxychloride glass systems remain relatively limited, particularly regarding their structural role and their influence on radiation attenuation behavior. Therefore, the present study aims to explore the influence of chromium(III) chloride ($CrCl_3$) incorporation on the structural, mechanical, and radiation shielding properties of calcium borate glass and glass ceramics. In particular, this work seeks to elucidate the role of Cr ions, in conjunction with chlorine species, in modifying the glass network and enhancing the attenuation performance of the material. By employing theoretical modeling and established computational frameworks, the radiation shielding parameters, including attenuation coefficients and related protection metrics, are systematically evaluated. The outcomes of this study provide new insights into the potential of oxychloride-modified borate glass systems as promising candidates for the design of next-generation lead-free radiation shielding materials.

Experimental method

Samples preparation

A series of glass samples was synthesized via the sol-gel method using the following precursor materials, purchased from Sigma-Aldrich with 99.5% purity: boric acid (H_3BO_3), calcium carbonate ($CaCO_3$), and chromium chloride ($CrCl_3\ 6H_2O$) as sources of B_2O_3, CaO, and $CrCl_3$, respectively. The precise amounts of each material were carefully weighed according to the glass compositions (Table 1) using an analytical balance with an error margin of ± 0.0002 g. Each component was dissolved separately in double-distilled water in individual beakers, with continuous magnetic stirring until the solution became transparent. The calcium carbonate ($CaCO_3$) was

Sample code	Glass compositions (mol%)
0CrCaB	$0CrCl_3$-55CaO-45B_2O_3
1CrCaB	$1CrCl_3$-55CaO-44B_2O_3
2CrCaB	$2CrCl_3$-55CaO-43B_2O_3
3CrCaB	$3CrCl_3$-55CaO-42B_2O_3

Table 1. Names of samples and glass composition with mol percentage (mol%).

treated with a few drops of hydrochloric acid (HCl) to facilitate the formation of a transparent sol. Once all individual sols had reached transparency, they were combined in a single beaker and stirred continuously to ensure uniformity. The resulting sol was placed in a thermal oven at 60 °C for 5 days until a gel formed. After the gel formed, the temperature was increased to 120 °C and maintained for 24 h to fully dry the gel, yielding a fine powder. Finally, to remove impurities, the obtained glass powder was calcined at 500 °C for 4 h and then the temperature was raised to 700 °C for 2 h.

Measurements and techniques

In this study, a set of instruments was utilized to characterize the prepared samples, as follows:

X-ray diffraction (XRD) spectroscopy

X-ray diffraction (XRD) measurements were carried out using a Rigaku SmartLab X-ray diffractometer operating with Cu Kα radiation (λ = 1.5406 Å) at 40 kV and 50 mA. The diffraction patterns were recorded over a 2θ range of 5°–80° with a step size of 0.01° and a scan speed of 50° min^{-1}. The samples were prepared as fine powders and analyzed to investigate their structural characteristics and to identify the presence of amorphous and crystalline phases.

Fourier transform infrared spectroscopy (FTIR)

FTIR spectra were recorded using a BRUKER INVENIO-S spectrometer operating in ATR mode. The measurements were carried out on the powdered samples over the wavenumber range of 400–4000 cm^{-1}. This analysis was conducted to investigate the functional groups present in the prepared glass samples.

Field emission scanning electron microscopy (FE-SEM)

Field Emission Scanning Electron Microscopy (NRC, QUANTA FEG250, 30 kV) coupled with Energy-Dispersive X-ray Spectroscopy (EDX) was employed to investigate the surface morphology and elemental composition of the synthesized glass-ceramic samples.

Measurement of density, molar volume, free volume, and packing density

At room temperature, Xylene was used as the immersion liquid to determine the density (D) of all samples using Archimedes' principle according to Eq. 1[27]. To ensure high accuracy and reproducibility, each sample was measured in triplicate, and the average value of the three measurements was reported as the final density. Based on the measured densities, additional physical properties such as molar volume (V_m), packing density (P_d), and free volume (V_f) were calculated using the following appropriate formulas[28–30]:

$$D = \frac{\text{Weight of glass in the air}}{\text{Weight of glass in the air} - \text{Weight of glass in the liquid}} \times \text{Density of the Xylene} \tag{1}$$

$$V_m = \sum \frac{M_i n_i}{D} \tag{2}$$

$$P_d = \sum \frac{x_i V_i}{V_m} \tag{3}$$

$$V_f = V_m - \sum x_i V_i \tag{4}$$

Mechanical properties

The Makishima–Mackenzie theory is used in this work to theoretically evaluate the mechanical properties of binary calcium borate glasses with varying concentrations of $CrCl_3$, based on the samples heat-treated at 500 °C, where the amorphous nature of the glasses was preserved[31–34]. Makishima–Mackenzie model depended on the dissociation energy (G_t, (KJ/cm^3)) and packing density (V_t), which are evaluated according to the following equations, respectively[35,36]:

$$G_t = \sum x_i G_i \tag{5}$$

$$V_t = \frac{D_{glass}}{M_w} \sum_i x_i V_i \tag{6}$$

where x_i, $V_i, and\ G_i$, represent the molar fraction, packing factor, and the dissociation energy of the i^{th} compounds constituting the studied glasses, respectively.

According to their coordination number, borate glasses are known to have two structural units: BO_4 and BO_3. In this case, the dissociation energy $G_{i(B2O3)}$ for B_2O_3 considers the coordination change and is represented by:

$$G_{i\,(B2O3)} = N_4 G_4 + (1 - N_4) G_3 \tag{7}$$

where N_4 represents the ratio of BO_4 to BO_3 units, and the G_4 and G_3 represent the dissociation energy per unit volume for BO_4 and BO_3 groups, respectively. The values of dissociation energy (G_i, KJ/cm^3) for B_2O_3, CaO, and $CrCl_3$ were listed in Table 2.

Based on the dissociation energy values (G_t), and packing density (V_t) parameters, the Young's moduli (*Y*, GPa), bulk modulus (*B*, GPa), longitudinal (*L*, GPa), shear modulus (*S*, GPa), and microhardness (*H*, GPa),

Component	Coordination number	Dissociation energy (G_i, KJ/cm^3)
B_2O_3	4	77.8224
B_2O_3	3	16.4
CaO	–	64.852
$CrCl_3$	–	750.69

Table 2. Dissociation energy (G_i, KJ/cm^3) and coordination number of the used oxides.

Eq. no.	Parameter	Abbreviations	Unit	Equation
8	Young's modulus	Y	GPa	$Y = 2\ G_t\ V_t$
9	Bulk modulus	B	GPa	$B = 2.4\ G_t\ V_t^2$
10	Shear modulus	S	GPa	$S = \frac{3BY}{(9B-Y)}$
11	Longitudinal modulus	L	GPa	$L = B + \frac{4}{3}S$
12	Poisson ratio	σ		$\sigma\ = 0.5 - \frac{1}{7.2V_t}$
13	Microhardness	H	GPa	$H = \frac{Y-2\sigma\ Y}{(6+6\sigma\ )}$

Table 3. Expressions, abbreviations, and units used to evaluate elastic moduli.

Eq. no.	Parameter	Abbreviations	Unit	Equation
14	Linear attenuation coefficient	*LAC*	cm^{-1}	$\frac{I}{I_0} = e^{-\mu\ t}$
15	Mass attenuation coefficient	*MAC*	cm^2/g	$\mu_{\ m} = \frac{\mu}{Density\ of\ the\ glass\ sample\ (\rho\ )}$
16	Mean free path	*MFP*	cm	$MFP = \frac{1}{\mu}$
17	Half value layer	*HVL*	cm	$HVL = \frac{\ln(2)}{\mu}$
18	Tenth value layer	TVL	cm	$TVL = \frac{\ln(10)}{\mu}$
19	Transition factor	TF	%	$\frac{I}{I_0} = 100{*}e^{-\mu\ t}$

Table 4. Parameters, abbreviations, units, and expressions used to evaluate the shielding efficiency of all the prepared samples.

as well as Poisson ratio (σ) were determined utilizing the following Eqs. (8–13), which are listed in Table 3, respectively[34,37]:

Shielding parameters evaluation

The shielding parameters were calculated theoretically using the Phy-X/PDS program over an energy range from 0.001 to 15 MeV[38]. These parameters are essential for evaluating the radiation shielding capabilities of the glass samples. The mass attenuation coefficient, linear attenuation coefficient, mean free path, half value layer, tenth value layer, and parameters were evaluated utilizing the following Eqs. (14–19, Table 4), respectively[39–43]:

Results and discussion

X-ray analysis

Figure 1a, b depicts the XRD patterns corresponding to calcium borate glass samples doped with chromium chloride (*x*CrCaB) of composition 55CaO-(45-*x*)B_2O_3-*x*$CrCl_3$, with *x* = 0, 1, 2, and 3 mol%. The fine glass powder was thermally treated at 500 °C for 4 h and then at 700 °C for 2 h. The XRD results revealed that the structural basis of these samples comprises both amorphous and semi-crystalline states. X-ray diffraction (XRD) analysis confirmed that the synthesized samples maintained an amorphous nature after being calcined at 500 °C for 4 h. However, upon increasing the temperature to 700 °C for 2 h, a noticeable transition to a glass-ceramic phase was observed. The samples with different concentrations of $CrCl_3$ (1CrCaB, 2CrCaB, and 3CrCaB) exhibited distinct changes compared to the sample without $CrCl_3$ (0CrCaB). Specifically, the XRD pattern for the 0CrCaB sample displayed a broad hump with only a few weak and poorly defined diffraction peaks. This indicates that this sample is largely amorphous with very limited crystallinity. In contrast, upon addition of $CrCl_3$, several sharp diffraction peaks were superimposed on the background, and their intensities increased with increasing $CrCl_3$ content. These sharp peaks indicate the formation of a crystalline phase within the glass matrix, suggesting that $CrCl_3$ acts as a crystalline agent. The formed crystalline phase was determined using the X'High Score/

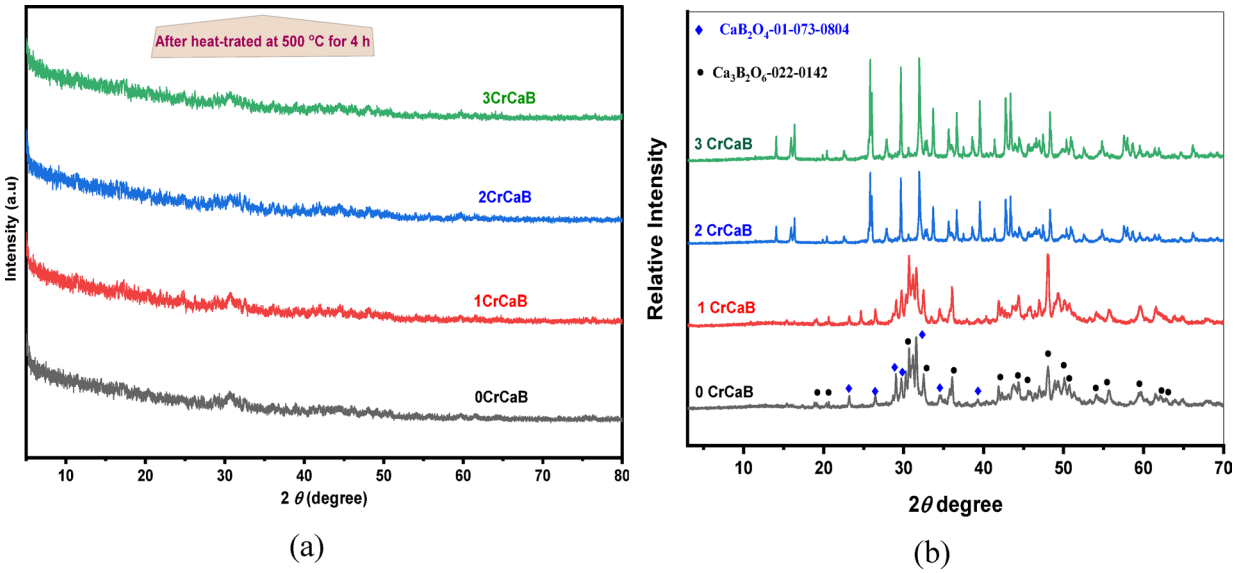

Fig. 1. (**a**), (**b**): XRD patterns of CaO-B_2O_3 glass samples doped with different concentrations of $CrCl_3$ (**a**) after heat-treated at 500 °C for 4 h, (**b**) after heat-treated at 700 °C for 2 h.

Plus program, corresponding to the calcium borate crystalline phase with the formula CaB_2O_4 (PDF. 01-073-0804), and $Ca_3B_2O_6$ (PDF. 022–0142). The formation of these crystalline phases within a glass matrix is highly significant because of their impact on the glass's physical and mechanical properties. The $Ca_3B_2O_6$ crystalline phase can enhance fracture toughness, stiffness, and hardness compared to the non-crystalline glassy phase. Due to the $CrCl_3$ content, nucleation and growth of these crystalline phases result in a composite-like structure that combines the strength of crystals with the flexibility of glass. The formation of these crystalline phases indicates a partial devitrification of the glass matrix. Crystallization typically results in a more ordered, compact atomic arrangement than glass's amorphous structure, thereby improving the material's overall shielding efficiency.

FTIR interpretation

Figure 2 presents the FTIR spectra of 0CrCaB, 1CrCaB, 2CrCaB, and 3CrCaB glass samples under different thermal treatment conditions: (a) as-prepared samples dried at 120 °C for 24 h, (b) samples heat-treated at 500 °C for 4 h, and (c) samples heat-treated at 700 °C for 2 h. A noticeable difference is observed between the spectra of the dried samples (Fig. 2a) and those of the heat-treated samples (Fig. 2b and c). In the as-prepared sample, several absorption bands associated with nitrate groups (NO_3^-) are detected, which originate from the precursor salts used during the sol–gel synthesis. For instance, nitrate units (NO_3^-) were detected at about 820 cm^{-1} and 1279 cm^{-1} which are assigned to the symmetric vibrations of NO_3^-[44,45]. Upon heat treatment at 500 °C and 700 °C, these nitrate-related bands disappear, indicating the thermal decomposition and elimination of nitrate species. This process facilitates the progressive development and stabilization of the borate glass network structure. In addition, a noticeable difference can be observed between the spectra shown in Fig. 2b and c. In Fig. 2b, the absorption bands appear relatively broad, which is characteristic of a predominantly amorphous structure. In contrast, the FTIR spectra in Fig. 2c exhibit sharper and partially split peaks, indicating a higher degree of structural ordering. This change can be attributed to the transition from an amorphous structure to a partially crystalline glass–ceramic phase upon heat treatment at 700 °C, which is consistent with the crystallization behavior observed in the XRD results. It was also observed that several noticeable changes occur in the FTIR spectra upon incorporation of $CrCl_3$. The splitting and sharpness of the FTIR bands become more pronounced with increasing $CrCl_3$ content, particularly in the fingerprint region, suggesting the possibility of forming a polycrystalline phase. This suggestion is confirmed by the XRD data shown in Fig. 1. The changes in the FTIR band positions, splitting, and intensity correspond to changes in the borate glass network connectivity. The FTIR bands in the low wavenumber range (400–600 cm^{-1}) are associated with cation vibrations[46]. The band at about 700 cm^{-1} is assigned to the asymmetric vibration mode of BO_3 units[47]. The bands that appear in the range 1200–1600 cm^{-1} correspond to the symmetric vibrational mode of BO_3 units[48]. The vibration mode associated with BO_4 units typically occurs in the 850–1200 cm^{-1} range. The FTIR absorption bands located at 3440 cm^{-1} and 1640 cm^{-1} are generally attributed to vibrations of H_2O and hydroxyl (OH) groups[49]. The deconvolution process was carried out to facilitate the FTIR bands (Fig. 2d, e with an accuracy of more than 99.085% (Fig. 2f), helping to determine the position and assignment of the bands as well as calculate the B_4 factor (B_4=B_4/(B_4+ B_3)), as shown in Fig. 3. The associated band positions and assignments are tabulated in Table 5. The deconvolution process is also used to calculate the ratio of B_3 and B_4 units for the total values of B_3+ B_4 units, as evidence in Table 6. In conventional borate glass, when the modifier content exceeds 40 mol%, N_4 (the fraction of BO_4) typically decreases. Conversely, in this study, with high modifier content, B_4 increases with increasing $CrCl_3$ content due to the formation of Ca_2BO_4 and $Ca_3B_2O_6$ crystalline phases, as well as the form of CrO_4 units. Depending on their coordination environments, Cr^{3+} ions can act as network formers and modifiers.

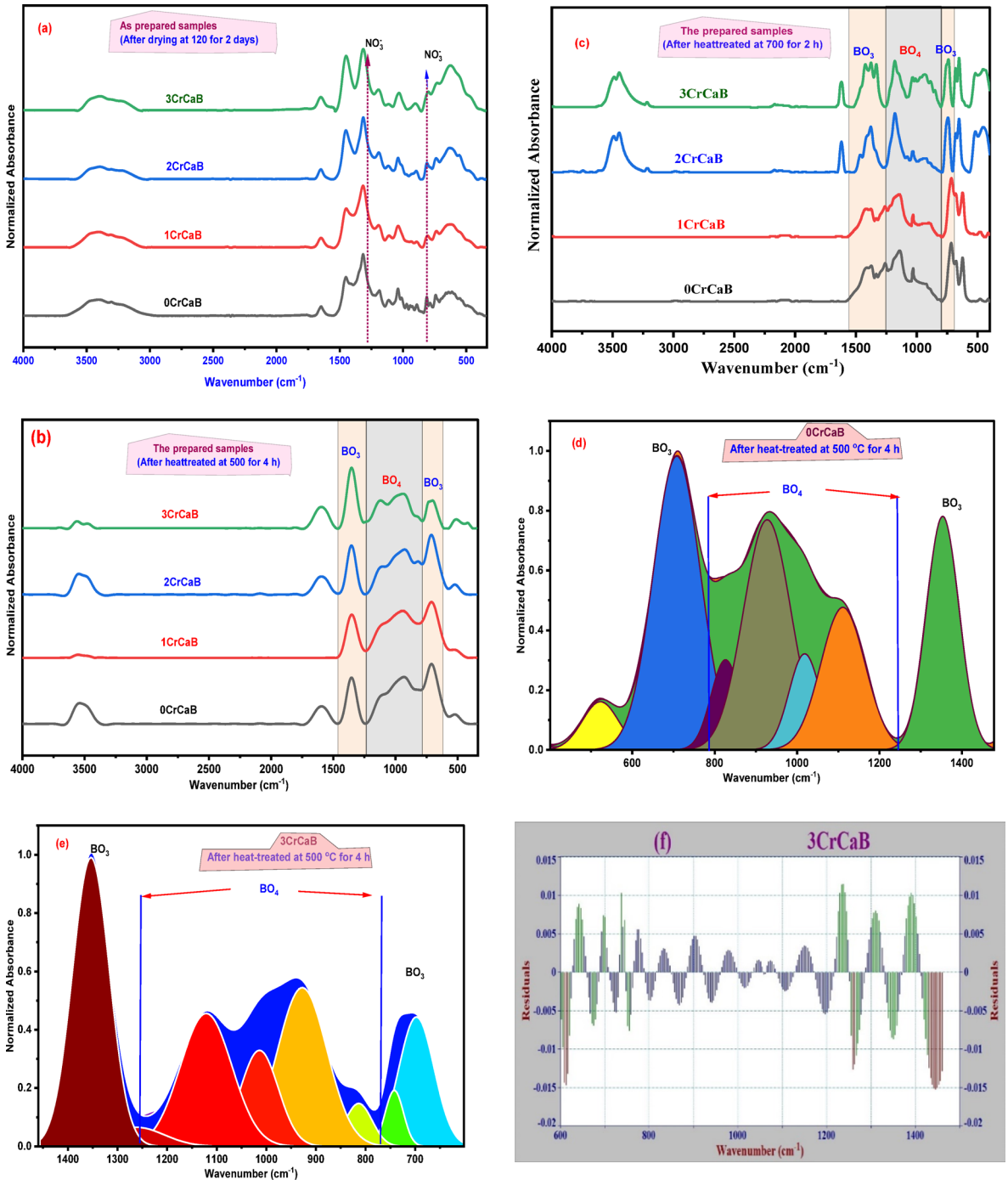

Fig. 2. (**a**)–(**d**): FTIR spectra versus wavenumber for 0CrCaB, 1CrCaB, 2CrCaB, and 3CrCaB as prepared samples (**a**), FTIR spectra for all samples after heat-treated at 500 °C for 4 h (**b**), FTIR spectra for all samples after heat-treated at 700 °C for 2 h (**c**), deconvoluted spectra for 0CrCaB and 3CrCaB as selected samples (**d**), (**e**), Residual graph of 3CrCaB sample, confirming the accuracy of the deconvolution process (**f**).

Cr^{3+} enters the borate network and stabilizes BO_4 units by sharing oxygen atoms, which promotes the formation of additional BO_4 units. Cr can play a former role, since CrO_4^{2-} units may form, which behave similarly to BO_4 units, favoring a tetrahedral, polymerized structure rather than allowing complete depolymerization. The formation of the crystalline phases (Ca_2BO_4 and $Ca_3B_2O_6$) removes some Ca^{2+} and Cr^{3+} ions from the glass network, leaving a remaining glass that behaves like one with a lower modifier content, which promotes higher B_4 values.

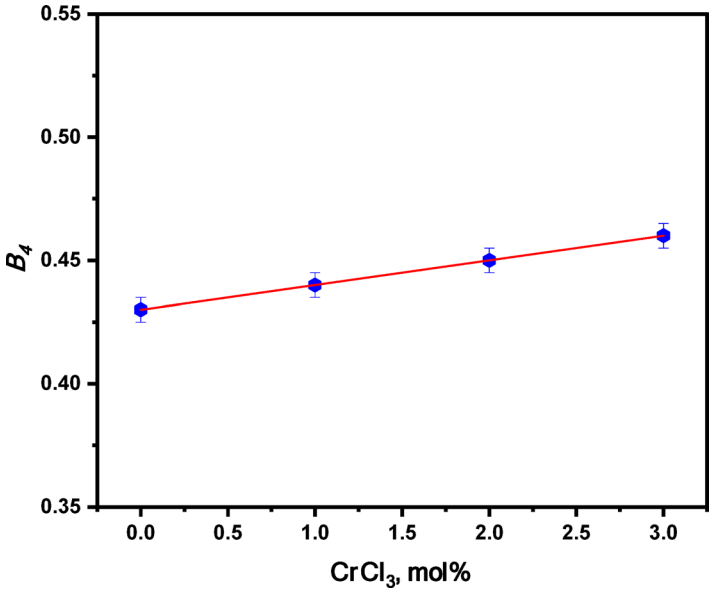

Fig. 3. B_4 factor versus $CrCl_3$ concentrations.

The band position	Assignments	References
400–600 cm^{-1}	Cation vibrations	[36]
700 cm^{-1}	Asymmetric vibration mode of BO_3 units	[37]
850–1200 cm^{-1}	Vibrational mode of BO_4 units	[38]
1200–1600 cm^{-1}	The symmetric vibrational mode of BO_3 units	[38]
1640 cm^{-1}	H_2O and hydroxyl (OH) groups	[39]
3440 cm^{-1}	H_2O and hydroxyl (OH) groups	[39]

Table 5. The associated FTIR band positions and their assignments.

Sample code	B_4	B_3
0CrCaB	0.436539	0.563461
1CrCaB	0.442314	0.557686
2CrCaB	0.454213	0.545787
3CrCaB	0.467701	0.532299

Table 6. Values of B_3 and B_4 units of all prepared samples.

Field emission scanning electron spectroscopy (FE-SEM)

The FE-SEM micrographs and EDX spectra of the undoped (0CrCaB) and $CrCl_3$-doped (3CrCaB) glass ceramics heat-treated at 700 °C for 2 h are presented in Figs. 4 and 5. The SEM images clearly demonstrate the distinct surface morphologies between the undoped and doped samples. As shown in Fig. 4a, the micrograph of the undoped glass (0CrCaB) shows a relatively smooth, dense surface with large, interconnected clusters, indicative of a predominantly amorphous glassy structure. In certain regions, occasional bright contrast spots and small angular fragments are observed along the edges, which may correspond to a minor fraction of nano- or micro-crystalline phases embedded within the amorphous matrix. Overall, the morphology is primarily amorphous, with traces of crystallinity, consistent with the weak, poorly defined reflections observed in the XRD pattern.

In contrast, the SEM micrograph of the $CrCl_3$-doped sample (3CrCaB, Fig. 5a) reveals smaller, more irregularly shaped particles featuring sharper boundaries and faceted surfaces. This observation indicates that the addition of $CrCl_3$ promotes partial crystallization within the glass matrix, leading to a mixed morphology comprising both amorphous regions and crystalline-like domains. The doped sample exhibits a rougher, more heterogeneous surface compared to the undoped glass's smoother, compact morphology. These results suggest that chromium incorporation alters the microstructure, facilitating the nucleation and growth of crystalline phases within the glassy matrix.

Energy-dispersive X-ray (EDX) analysis of the undoped and $CrCl_3$-doped samples confirmed the presence of the constituent elements of the glass system, as shown in Figs. 4b and 5b. For the undoped sample, the detected

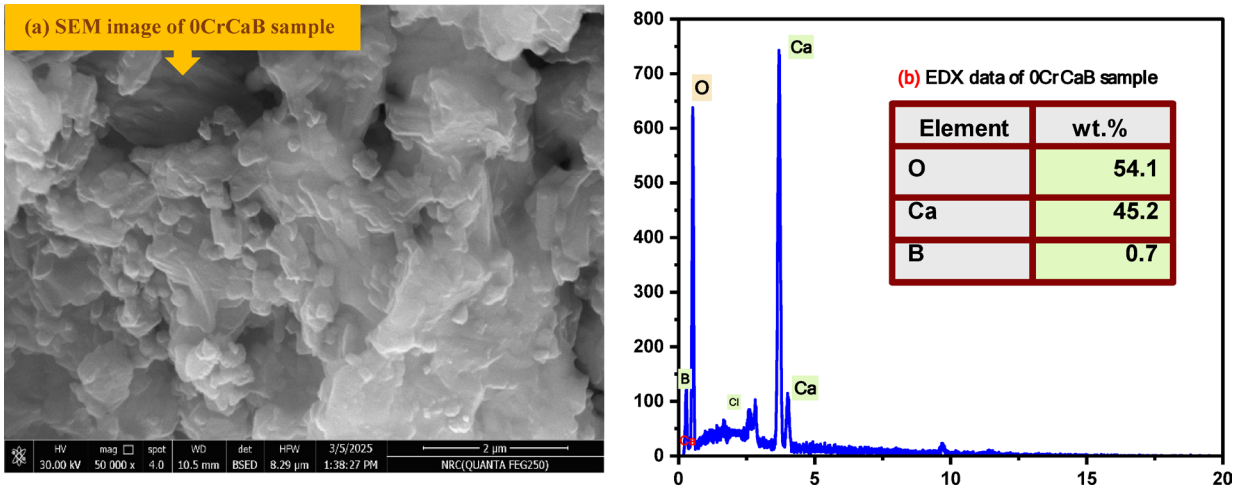

Fig. 4. SEM micrograph at 50000x magnification (**a**), and EDX spectrum and results (**b**) of 0CrCaB sample after heat-treated at 700 °C for 2 h.

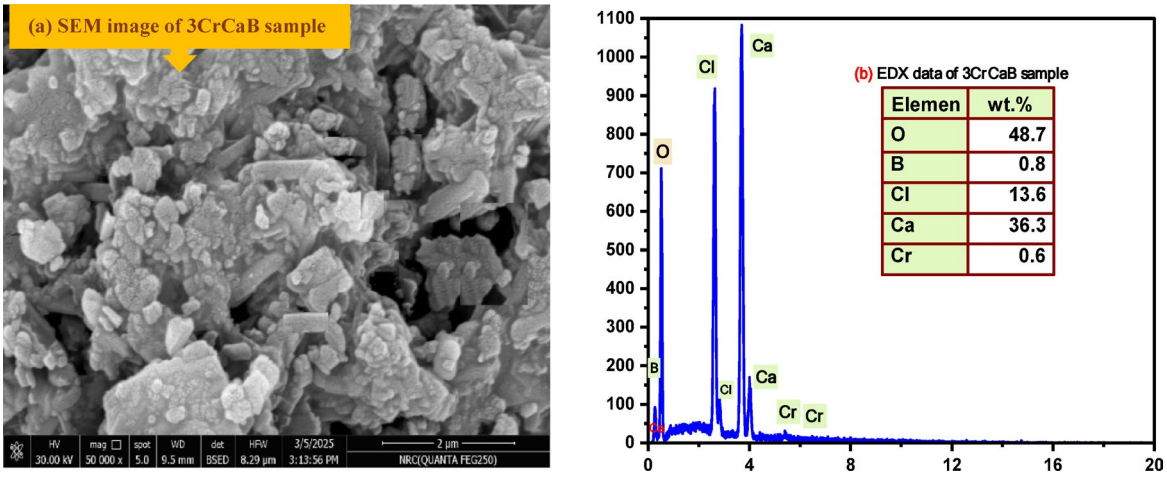

Fig. 5. SEM micrograph at 50000x magnification (**a**), and EDX spectrum and results (**b**) of 3CrCaB sample after heat-treated at 700 °C for 2 h.

elements were Ca, O, and B, with a minor Cl signal likely originating from residual HCl used during sample preparation. In contrast, the EDX spectrum of the $CrCl_3$-doped sample (3CrCaB) revealed the presence of Ca, B, O, Cl, and Cr, confirming the successful incorporation of chromium and chlorine species into the glass matrix.

Density, packing density, molar volume, and free volume

Figure 6 presents the variation of density, molar volume, packing density, and free volume as a function of $CrCl_3$ concentration. It can be observed that the density increases with increasing $CrCl_3$ content, rising from 2.57 g cm^{-3} for the 0CrCaB sample to 3.11 g cm^{-3} for the 3CrCaB sample. In contrast, the molar volume decreases from 24.19 cm^3 mol^{-1} for the 0CrCaB sample to 20.85 cm^3 mol^{-1} for the 3CrCaB sample, as summarized in Table 7. The incorporation of $CrCl_3$ into the borate glass network increased the fraction of B_4 units, which have a higher atomic packing density than B_3 units. This structural transformation leads to an overall increase in glass density. The enhanced compactness of the glass network consequently reduces the molar volume. This reduction arises from the higher atomic coordination and the decreased interatomic spacing within the matrix, which together compact the structure. The B_4 tetrahedra exhibit a more compact configuration than the planar B_3 units, resulting in tighter atomic packing. Additionally, Cr^{3+} ions can function as network intermediates or modifiers, promoting further cross-linking within the structure. As a result, the packing density increases from 0.6 to 0.7, indicating a more efficiently packed network. The corresponding free volume, representing the unoccupied space within the glass matrix, decreases markedly from 9.68 to 6.32 cm^3 mol^{-1}. This reduction signifies a more tightly packed atomic arrangement with fewer voids and lower structural disorder. The simultaneous increase in density and packing density, coupled with reductions in both molar and free volumes, reflects the progressive ordering and densification of the glass structure. This observation aligns with the XRD results, which indicate

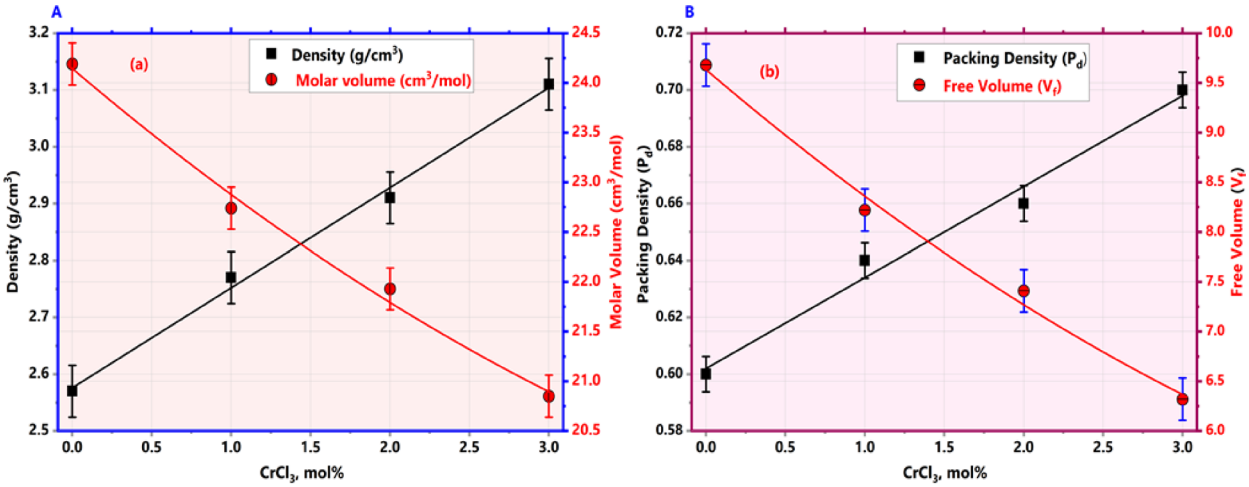

Fig. 6. (**a**) Density and molar volume, and (**b**) packing density and free volume of all prepared samples as a function of $CrCl_3$ content.

Physical parameters	Sample code			
	0CrCaB	1CrCaB	2CrCaB	3CrCaB
Density (d_s)gcm^{-3}±0.0002	2.57	2.77	2.91	3.11
Molar volume (V_m) cm^{3}mol^1±0.0001	24.19	22.74	21.93	20.85
Packing density (V_t)	0.60	0.64	0.66	0.70
Free volume (V_f) cm^3/mol	9.68	8.22	7.41	6.32

Table 7. Calculated values of density, molar volume, packing density, and free volume of all investigated samples.

Sample Code	G_t	Y (GPa)	B (GPa)	S (GPa)	L (GPa)	H (GPa)	σ
0CrCaB	55.115	66.137	47.619	26.069	82.377	4.0230	0.269
1CrCaB	62.345	79.802	61.288	31.100	102.755	4.4994	0.283
2CrCaB	69.731	92.045	72.899	35.688	120.484	5.0068	0.290
3CrCaB	77.143	108.000	90.720	41.488	146.037	5.4878	0.302

Table 8. Mechanical parameters of undoped and $CrCl_3$ doped $CaO\text{-}B_2O_3$ glasses.

an enhancement in crystallinity upon $CrCl_3$ incorporation. As the crystalline content increases, the elimination of disordered regions and interstitial voids contributes to a denser, more compact structure in glass ceramics.

Mechanical properties

The mechanical performance of glass and glass–ceramic materials is a critical factor for their application in radiation shielding, where both high mechanical strength and effective attenuation capability are required. In the present study, the elastic properties of the prepared samples were theoretically evaluated using the Makishima–Mackenzie model, which is applies to amorphous glass systems. As confirmed by the XRD results, the samples heat-treated at 500 °C retained their amorphous structure, whereas partial crystallization was observed at higher heat-treatment temperatures (700 °C). Therefore, the mechanical properties were calculated based on the samples heat-treated at 500 °C. The Young's modulus (Y) and other related elastic parameters were determined using Eqs. (5–13). The calculated values are summarized in Table 8 and presented as a function of $CrCl_3$ concentration (mol%) in Fig. 7. With increasing $CrCl_3$ content, a significant enhancement in elastic moduli was observed. Specifically, Y increased from 66.137 to 108.00 GPa, B from 47.619 to 90.720 GPa, S from 26.069 to 41.488 GPa, and L from 82.377 to 146.037GPa. Similarly, the microhardness, H, increased from 4.0230 to 5.4878 GPa. Meanwhile, Poisson's ratio (σ) exhibited a moderate increase from 0.269 to 0.302 as the $CrCl_3$ concentration rose from 0 to 3 mol%. This enhancement in mechanical parameters can be attributed to increased formation of B_4 units, a higher average bond density per unit volume, and greater cross-linking within the glass network. Moreover, the incorporation of Cr^{3+} ions increases the Coulombic interaction energy within the glass-ceramic structure, further strengthening the network. The increase in all elastic moduli reflects the improved rigidity and compactness of the glass matrix. The total dissociation energy per unit volume (G_t) also

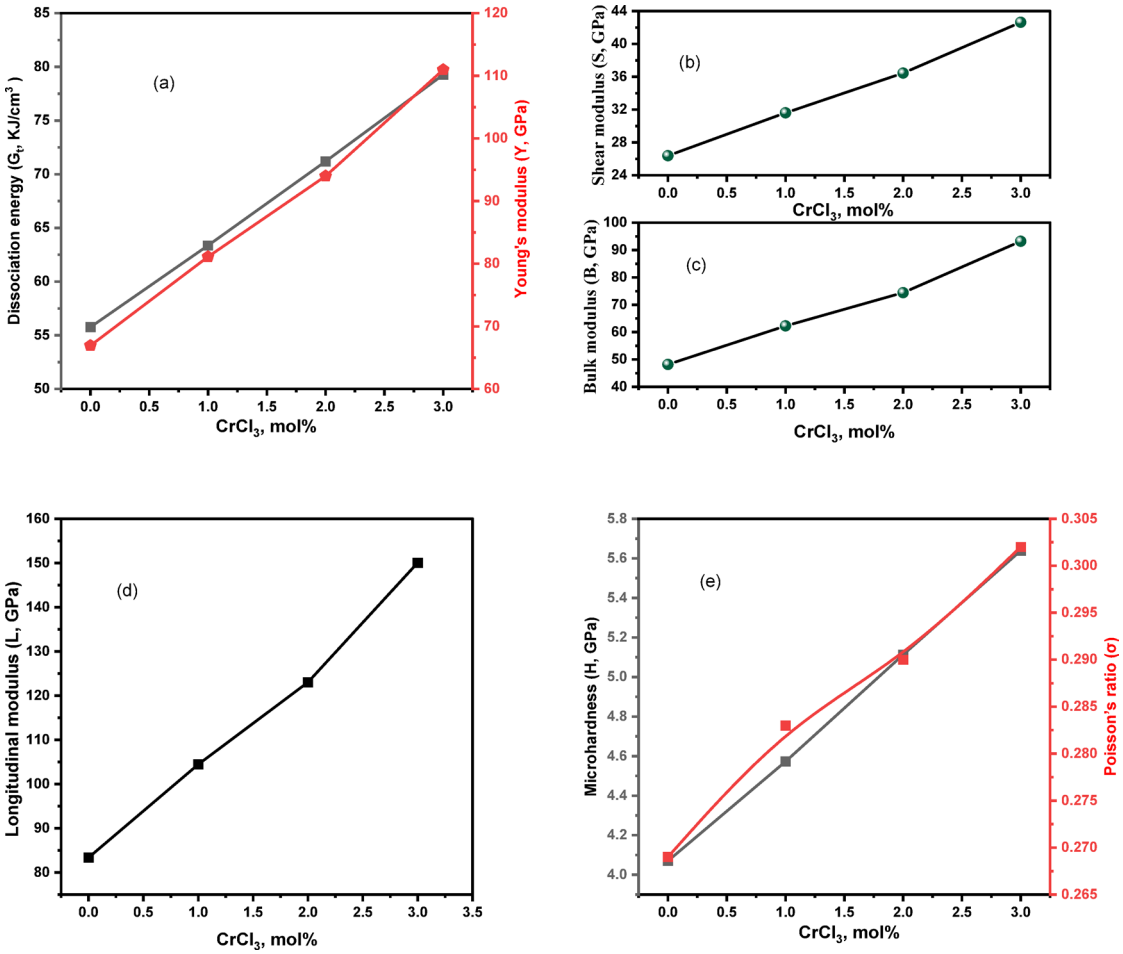

Fig. 7. Variation of (**a**) Young's modulus and dissociation energy, (**b**) bulk modulus, (**c**) shear modulus, (**d**) longitudinal modulus, and (**e**) microhardness and Poisson's ratio as a function of $CrCl_3$ content.

increased from 55.763 to 79.266 kJ cm^{-3}, supporting the strong correlation between molar volume and Young's modulus through both V_t and G_t parameters[50]. A minor discrepancy between the longitudinal and shear moduli (L and G) may arise from size-related effects. The microhardness results indicate consistent mechanical stability, suggesting a well-connected and robust glass network. Variations in Poisson's ratio (σ) provide further insight into network dimensionality: σ values in the range of 0.1–0.3 correspond to highly cross-linked structures, whereas higher values (0.4–0.5) indicate less cross-linking. The observed σ values (0.27–0.30) thus confirm a highly interconnected and mechanically stable glass-ceramic network in the present system.

Additionally, a comparison was made between the present results and previously reported data for various binary borate glasses, as illustrated in Fig. 8[28]. The incorporation of small amounts of modifiers such as Na_2O, Li_2O, Cs_2O, PbO, and K_2O into B_2O_3 has been shown to enhance Young's modulus (Y). This enhancement is typically attributed to the formation of B_4 structural units and the increased ionic attraction between adjacent layers of B_3 triangles following the disruption of B–O bonds. Compared with these earlier studies, the current glass system exhibits significantly higher Y values, which can be attributed to the higher dissociation energy of CaO. Furthermore, the addition of $CrCl_3$ further increases the Young's modulus due to its high dissociation energy per unit volume (G_t). These findings suggest that network modifiers exhibiting high G_t values are effective in developing glass systems with enhanced mechanical rigidity and elevated Young's modulus.

Radiation Shielding properties

In medical facilities, both X-rays and gamma rays are commonly used for diagnostic imaging. During exposure to such low-intensity radiation, various protective measures are typically implemented to safeguard healthier workers and patients from scattered radiation. Among these measures is the use of radiation shielding glass, which serves as a barrier to minimize radiation exposure while allowing visibility and communication between areas. In this regard, the gamma energy was divided into five regions, ranging from 0.015 to 0.1 MeV as the lower region to energies above 10 MeV corresponding to the high-energy region[51], since lower gamma-ray energies are used in diagnostic imaging. X-rays used in medical imaging typically range in energy from 0.01 to 0.15 MeV, whereas gamma rays used in the energy range from 0.1 to 1.5 MeV, depending on the radionuclide[52,53]. Therefore, to enhance the safety of both patients and healthcare professionals, researchers are encouraged to

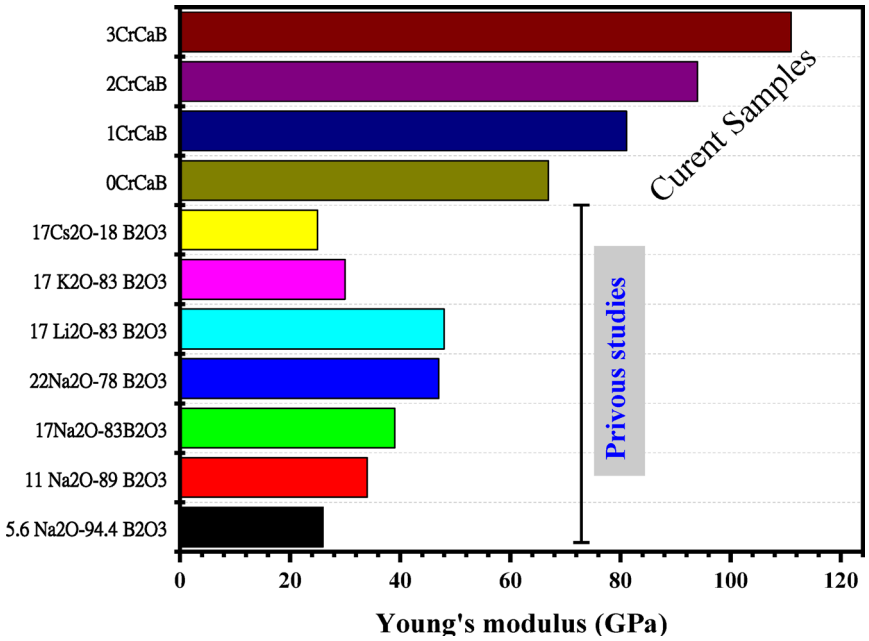

Fig. 8. Comparison of Young's modulus values between the present study and previously reported borate glass systems.

explore the development of specialized protective glass for use across various settings, including protective eyewear to shield against harmful radiation. To evaluate the glass under study (*x*CrCaB) for its effectiveness, several shielding attenuation parameters are theoretically calculated, including the mass attenuation coefficient, half-value and tenth-value layers, and the mean free path factors.

Mass attenuation coefficient (MAC) and linear attenuation coefficient (LAC)

The mass attenuation coefficient (MAC) represents the extent to which a material can attenuate a photon beam per unit mass density. Fundamentally, it quantifies the probability of photon interactions within the shielding medium, thereby serving as a crucial parameter in the design of effective radiation protection materials. The linear attenuation coefficient (LAC) describes the attenuation of photons per unit thickness of the shielding material. Unlike MAC, the LAC depends directly on the physical density of the medium. It provides practical information about how rapidly the photon intensity decreases as it passes through a given thickness of the material. Consequently, the LAC is widely used to evaluate the shielding efficiency and to determine the required thickness of materials for radiation protection applications. A higher MAC value indicates a greater likelihood of photon absorption or scattering, thereby enhancing the material's efficiency as a radiation shield. In general, photons interact with matter through five primary mechanisms: coherent scattering, the photoelectric effect, Compton scattering, electron–positron pair production, and photon disintegration[54,55]. Each of these processes contributes to the overall attenuation behavior, underscoring the significance of MAC as a key descriptor of a material's radiation shielding performance. Figure 9a presents the variation of the mass attenuation coefficient (MAC) for all synthesized glass samples as a function of photon energy in the range of 0.015–1.5 MeV. As shown in Fig. 9a and in the MAC and LAC values listed in Table 9, both MAC and LAC exhibit relatively high values at low photon energies and decrease progressively with increasing energy. This behavior can be attributed to the dominance of the photoelectric absorption process at lower photon energies, where the probability of interaction between incident photons and the atomic constituents of the glass matrix is significantly higher. The $CrCl_3$-containing samples exhibit higher MAC and LAC values compared with the undoped sample, indicating that the incorporation of $CrCl_3$ enhances the attenuation capability of the glass system. As the $CrCl_3$ concentration increases, boron (a low atomic number element) is progressively replaced by chromium, which has a higher atomic number and greater photon interaction probability. This substitution increases the attenuation efficiency of the material toward gamma radiation. Consequently, the mass attenuation coefficient (μ/ρ) increases with increasing $CrCl_3$ content. Among all prepared compositions, the 3CrCaB sample shows the highest attenuation values, confirming the intermediate role of Cr ions in the glass network.

Half value layer (HVL), tenth value layer (TVL), and mean free path (MFP)

The thickness of a shielding material plays a pivotal role in determining its effectiveness for specific radiation protection applications. The half-value layer (HVL) and tenth-value layer (TVL) represent the material thicknesses required to reduce the incident photon intensity by 50% and 10%, respectively[27]. In contrast, the mean free path (MFP) refers to the average distance that a photon travels within a material before undergoing an interaction such as absorption or scattering, thereby indicating the average spacing between successive photon interactions in the shielding medium[56]. These parameters are essential in medical and industrial contexts, as

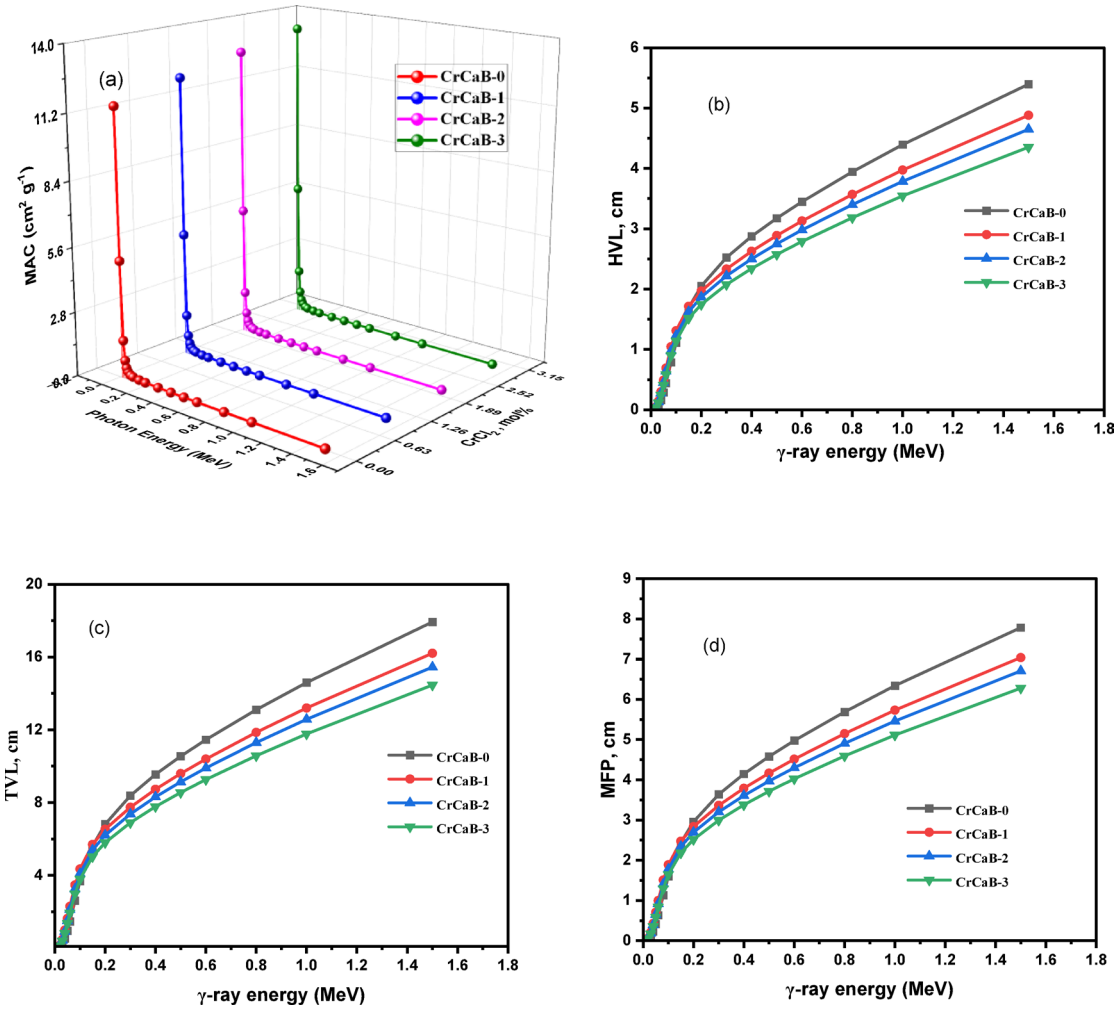

Fig. 9. Variations of (**a**) MAC ($cm^2\ g^{-1}$), (**b**) HVL (cm), (**c**) TVL (cm), and (**d**) MFP (cm) values for all synthesized glass samples as a function of photon energy ranging from 0.015 to 1.5 MeV.

they guide the assessment of safe exposure levels and the design of protective barriers to minimize radiation doses. Materials exhibiting lower HVL and TVL values are generally more efficient attenuators.

Figure 9b–d illustrates the variations of HVL, mean free path (MFP), and TVL with photon energy. Among the investigated glasses, the 3CrCaB sample demonstrated the lowest HVL and TVL values, indicating superior shielding performance. Specifically, the HVL of the 0CrCaB glass ranges from 0.023 cm at 0.015 MeV to 5.265 cm at 1.5 MeV, whereas that of the 3CrCaB sample varies from 0.017 cm at 0.015 MeV to 4.352 cm at 1.5 MeV. The MFP, which represents the average distance a photon travels in the material before undergoing an interaction, is plotted as a function of photon energy in Fig. 9d. At 0.2 MeV, the MFP values range from 2.522 to 3.063 cm, with the 3CrCaB glass achieving the minimum (2.522 cm). This low MFP indicates a higher probability of photon–matter interactions, suggesting that photons lose energy over shorter distances within the glass, thereby increasing its attenuation efficiency. The incorporation of $CrCl_3$ into the glass matrix leads to increased density, improved packing efficiency, and stronger mechanical properties, which contribute to the structural stability that contribute to improved radiation attenuation performance. In particular, replacing B_2O_3 with $CrCl_3$ introduces chromium ions with higher atomic number and mass, which increases the interaction probability between gamma photons and the material. As a result, the mass attenuation coefficient increases, while parameters such as HVL, TVL, and MFP decrease, indicating enhanced shielding efficiency. These combined effects make the $CrCl_3$-doped samples more effective for radiation shielding compared to the undoped glass composition. Collectively, the HVL, TVL, and MFP parameters provide a comprehensive framework for evaluating and designing radiation shielding materials. While HVL and TVL offer practical insights into the required shielding thickness, MFP provides a fundamental understanding of photon transport and interaction mechanisms within the material.

The mechanical properties and mass attenuation behavior of $CrCl_3$-modified borate glass are closely interrelated through the material's underlying structural characteristics. The observed differences in Young's modulus, shear modulus, bulk modulus, and mass attenuation coefficient between the two borate glass compositions, namely $45B_2O_3$–55CaO and $42B_2O_3$–55CaO–$3CrCl_3$, can be attributed to structural modifications induced by the

Photon energy (MeV)	MAC (cm^2/g)				LAC (cm^{-1})			
	0CrCaB	1CrCaB	2CrCaB	3CrCaB	0CrCaB	1CrCaB	2CrCaB	3CrCaB
1.50×10^{-2}	11.536	12.003	12.463	12.914	29.648	33.249	36.266	40.163
2.00×10^{-2}	5.101	5.306	5.508	5.707	13.108	14.698	16.029	17.748
3.00×10^{-2}	1.663	1.726	1.788	1.849	4.275	4.782	5.204	5.751
4.00×10^{-2}	0.803	0.830	0.857	0.883	2.065	2.300	2.493	2.745
5.00×10^{-2}	0.492	0.506	0.519	0.533	1.264	1.400	1.511	1.656
6.00×10^{-2}	0.351	0.359	0.367	0.375	0.903	0.995	1.068	1.166
8.00×10^{-2}	0.235	0.238	0.241	0.245	0.603	0.659	0.702	0.760
1.00×10^{-1}	0.189	0.190	0.192	0.194	0.485	0.528	0.559	0.602
1.50×10^{-1}	0.145	0.146	0.146	0.147	0.374	0.404	0.426	0.456
2.00×10^{-1}	0.127	0.127	0.127	0.127	0.326	0.352	0.371	0.396
3.00×10^{-1}	0.107	0.107	0.107	0.107	0.276	0.297	0.312	0.334
4.00×10^{-1}	0.095	0.095	0.095	0.095	0.245	0.264	0.277	0.296
5.00×10^{-1}	0.087	0.087	0.087	0.087	0.223	0.240	0.252	0.269
6.00×10^{-1}	0.080	0.080	0.080	0.080	0.206	0.222	0.233	0.248
8.00×10^{-1}	0.070	0.070	0.070	0.070	0.180	0.194	0.204	0.218
1.00×10^{0}	0.063	0.063	0.063	0.063	0.162	0.174	0.183	0.196
1.50×10^{0}	0.051	0.051	0.051	0.051	0.132	0.142	0.149	0.159
2.00×10^{0}	0.044	0.044	0.044	0.044	0.114	0.123	0.129	0.138
3.00×10^{0}	0.036	0.036	0.036	0.036	0.093	0.100	0.105	0.112
4.00×10^{0}	0.032	0.032	0.032	0.032	0.081	0.088	0.092	0.098
5.00×10^{0}	0.029	0.029	0.029	0.029	0.074	0.080	0.084	0.090
6.00×10^{0}	0.027	0.027	0.027	0.027	0.069	0.074	0.078	0.084
8.00×10^{0}	0.024	0.024	0.025	0.025	0.063	0.068	0.071	0.077
1.00×10^{1}	0.023	0.023	0.023	0.023	0.059	0.064	0.068	0.073
1.50×10^{1}	0.022	0.022	0.022	0.022	0.055	0.060	0.063	0.068

Table 9. MAC and LAC values of the prepared samples at different photon energies.

presence of $CrCl_3$. The base glass composition containing 45 mol% B_2O_3 exhibits lower mechanical moduli (Young's, shear, and bulk) due to B_2O_3's inherent role as a glass network former, which generates a relatively open and flexible structure. High concentrations of B_2O_3 increase the number of BO_3 triangular units, resulting in lower cross-link density and weaker mechanical integrity than in more polymerized networks. Upon the incorporation of 3 mol% $CrCl_3$ a significant enhancement in mechanical properties is observed. $CrCl_3$ acts as a network intermediate or partial former, introducing Cr–O bonds that are typically stronger and more rigid than B–O bonds.

Additionally, the incorporation of Cr ions is expected to enhance cross-linking within the glass network and reduce the concentration of non-bridging oxygens, thereby increasing the structural compactness and rigidity of the system. These structural modifications collectively contribute to the observed increase in the elastic parameters, including Young's modulus, shear modulus, and bulk modulus, in the $CrCl_3$–containing glasses. In contrast, the higher attenuation coefficient observed in the $CrCl_3$–ree glass ($45B_2O_3$–55CaO) can be attributed to its relatively open and more disordered network structure, which promotes internal friction and energy dissipation. The greater structural flexibility of this composition facilitates enhanced damping of acoustic and mechanical waves, resulting in higher attenuation. Conversely, the incorporation of $CrCl_3$ leads to a more rigid and compact network, thereby reducing internal friction and lowering the attenuation coefficient. Furthermore, the formation of crystalline phases within the glass matrix contributes to the development of a denser microstructure, which increases the probability of photon interaction with the material. The presence of these crystalline regions also improves the structural stability of the system and may enhance the effective atomic packing density.

A comparative Study with Conventional Materials

A comparative evaluation of the mass attenuation coefficients (MAC) and half-value layers (HVL) of the studied glass samples was performed, not only against previously investigated glass systems but also against conventional concrete shielding materials. This comparison provides a clearer understanding of the radiation shielding performance of the present samples, illustrating how they align with or surpass current shielding standards.

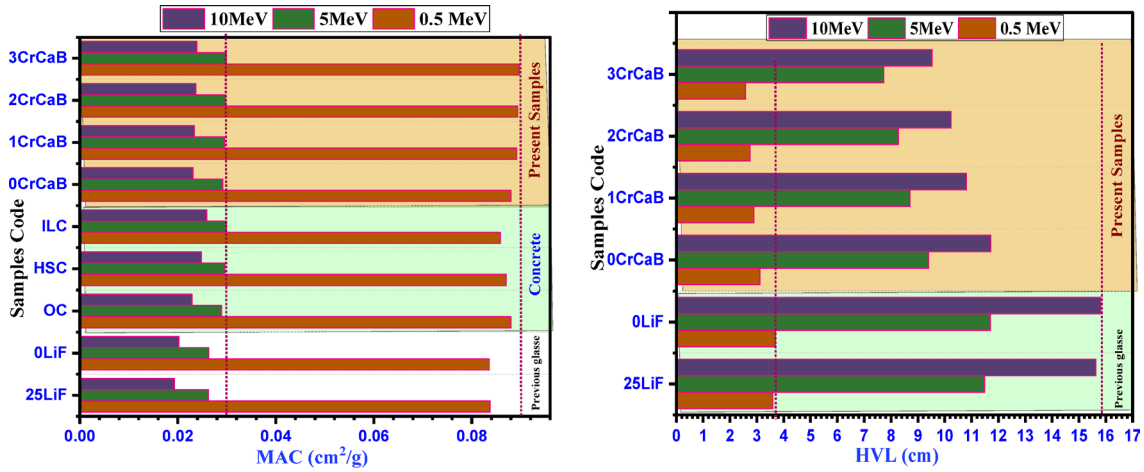

(a) (b)

Fig. 10. (**a**): MAC (cm^2/g) for all synthesized samples compared with reported borate glasses, 0LiF and 25LiF, as well as with OC, HSC, and ILC as reference samples. (**b**): HVL (cm) for all synthesized samples compared with reported borate glasses, 0LiF and 25LiF as reference samples.

Sample Code	MAC (cm^2/g)			HVL (cm)			
	0.5 MeV	5 MeV	10 MeV	0.5 MeV	5 MeV	10 MeV	
25LiF	0.08372	0.02625	0.01928	3.600	11.481	15.630	Previous Samples
0LiF	0.08357	0.02632	0.02022	3.686	11.703	15.812	
OC	0.088	0.0289	0.0229	–	–	–	Concrete samples
HSC	0.087	0.0296	0.0248	–	–	–	
ILC	0.0858	0.0299	0.0259	–	–	–	
0CrCaB	0.0880	0.0292	0.0231	3.111	9.400	11.713	Studied samples
1CrCaB	0.0892	0.0295	0.0234	2.888	8.706	10.810	
2CrCaB	0.0894	0.0297	0.0237	2.751	8.273	10.237	
3CrCaB	0.0897	0.0299	0.0239	2.576	7.729	9.532	

Table 10. Comparison of the mass attenuation coefficient (MAC, cm^2/g) and half-value layer (HVL, cm) of the synthesized samples with those of selected samples reported in previous studies.

Figure 10 presents the variations of the MAC (μ_m, $cm^2\ g^{-1}$) and HVL (cm) of the investigated glasses (0CrCaB, 1CrCaB, 2CrCaB, and 3CrCaB) in comparison with those of standard commercial concretes, Ordinary Concrete (OC), Hematite–Serpentine Concrete (HSC), and Ilmenite–Limonite Concrete (ILC), as well as previously reported glass systems (0LiB and 25LiB)[11]. The comparison was performed at photon energies of 0.5, 5, and 10 MeV, as reported in Refs[57,58]. As summarized in Table 10, the 3CrCaB glass exhibits a higher MAC and a lower HVL compared with OC, HSC, ILC, and the 0LiB and 25LiB glasses, demonstrating its superior γ-ray attenuation capability.

Conclusion

In this study, binary calcium borate glasses doped with chromium chloride ($CrCl_3$) were successfully synthesized via the sol–gel method and systematically characterized using X-ray diffraction (XRD), Fourier-transform infrared spectroscopy (FTIR), and field-emission scanning electron microscopy (FE-SEM). The density of the prepared samples was determined using Archimedes' principle, and related structural parameters, including molar volume, packing density, and free volume, were theoretically calculated. For the samples heat-treated at 500 °C, where the amorphous structure was preserved, the Makishima–Mackenzie model was applied to evaluate the mechanical properties. In addition, the Phy-X/PSD online software was used to assess the gamma-ray shielding performance of the investigated glasses. The main findings of this study are summarized as follows:

- $CrCl_3$-doped binary calcium borate glasses were successfully synthesized using the sol–gel method, confirming the feasibility of incorporating chromium chloride into the calcium borate glass system.

- Structural characterization (XRD and FTIR) revealed that the glasses heat-treated at 500 °C exhibited an amorphous structure. In contrast, partial crystallization was observed at a higher heat-treatment temperature (700 °C), indicating that $CrCl_3$ can promote crystallization within the glass matrix.
- The density of the prepared glasses increased from 2.57 to 3.11 g cm^{-3} with increasing $CrCl_3$ content due to the substitution of B_2O_3 by the heavier $CrCl_3$ component. In contrast, the related structural parameters such as molar volume, packing density, and free volume were correspondingly modified.
- The mechanical properties showed significant changes with increasing $CrCl_3$ concentration. Young's modulus increased from 66.137 to 108.00 GPa, bulk modulus from 47.619 to 90.720 GPa, shear modulus from 26.069 to 41.488 GPa, and microhardness from 4.023 to 5.4878 GPa.
- The gamma-ray shielding performance improved with $CrCl_3$ incorporation as indicated by higher mass attenuation coefficient (MAC) values and lower HVL, TVL, and MFP values.
- Among the investigated compositions, the 3CrCaB glass exhibited the best overall performance, combining enhanced mechanical strength and good gamma-ray attenuation capability.

These findings suggest that $CrCl_3$-modified calcium borate glasses may be suitable for radiation shielding applications.

Data availability

The datasets generated during and/or analyzed during the current study are available from the corresponding author on reasonable request.

Received: 8 November 2025; Accepted: 23 March 2026
Published online: 26 March 2026

References

1. Rammah, Y., Abouhaswa, A., Sayyed, M., Tekin, H. & El-Mallawany, R. Structural, UV and shielding properties of ZBPC glasses. *J. Non-cryst. Solids*. **509**, 99–105 (2019).
2. Kashif, I. & Ratep, A. Optical properties of borate glasses containing chromium and erbium oxide. *Appl. Phys. A*. **129** (7), 489 (2023).
3. Wright, A. C., Dalba, G., Rocca, F. & Vedishcheva, N. M. Borate versus silicate glasses: why are they so different? *Phys. Chem. Glasses-European J. Glass Sci. Technol. Part. B*. **51** (5), 233–265 (2010).
4. Bengisu, M. Borate glasses for scientific and industrial applications: a review. *J. Mater. Sci.* **51**, 2199–2242 (2016).
5. Lian, M., Wang, T. & Wei, C. Effect of B2O3 and basic oxides on network structure and chemical stability of borosilicate glass. *Ceramics* **7** (2), 516–529 (2024).
6. Lin, Y., Ren, W., Zhou, Z. & Chen, S. Degradation-controlling mechanisms in natural organic acid solutions of CaO–Al2O3–SiO2–B2O3 glass-ceramics by partially substituting Ca2 + with Ba2 + and Sr2+. *Ceram. Int.* **49** (16), 26860–26870 (2023).
7. Thind, K. et al. Compositional dependence of in-vitro bioactivity in sodium calcium borate glasses. *J. Phys. Chem. Solids*. **70** (8), 1137–1141 (2009).
8. Abdelghany, A. M. et al. Structural, optical and radiation shielding parameters of sodium aluminium borate glasses modified with chromium oxide. *Radiation Phys. Chem.* **207**, p110861. (2023). https://doi.org/10.1016/j.radphyschem.2023.110861
9. Udi, U. J., Yussof, M. M., Ayagi, K. M., Bedon, C. & Kamarudin, M. K. Environmental degradation of structural glass systems: A review of experimental research and main influencing parameters. *Ain Shams Eng. J.* **14** (5), 101970 (2023).
10. Mhareb, M. et al. Investigation of photon, neutron and proton shielding features of H3BO3–ZnO–Na2O–BaO glass system. *Nuclear Eng. Technol.* **53** (3), 949–959 (2021).
11. Abdelghany, A., Ramadan, R., Elbatal, H. & Madshal, M. Structural, optical, and shielding characteristics of CuO diborate glasses containing lithium fluoride or lithium oxide. *Results Chem.* **7**, 101299 (2024).
12. Gharghar, F., Madshal, M., Damrawi, G. E. & Abdelghany, M. Structural, physical and shielding attenuation properties of silicate glass ceramics containing copper sulfate. *Appl. Phys. A*. **131** (6), 1–13 (2025).
13. Madshal, M., El-Damrawi, G., Baiomy, M. E. & Behairy, A. Calcium Silicate Glass Ceramics Containing Chromium Sulfate: Structural, Optical, and Shielding Properties. *Arab. J. Sci. Eng.* **49** (7), 10147–10161 (2024).
14. Chandra, R. J., Shivamurthy, B., Kulkarni, S. D. & Kumar, M. S. Hybrid polymer composites for EMI shielding application-a review. *Mater. Res. Express*. **6** (8), 082008 (2019).
15. Dong, M., Xue, X., Yang, H. & Li, Z. Highly cost-effective shielding composite made from vanadium slag and boron-rich slag and its properties. *Radiat. Phys. Chem.* **141**, 239–244 (2017).
16. Zaid, M. et al. Influence of heavy metal oxides to the mechanical and radiation shielding properties of borate and silica glass system. *J. Mater. Res. Technol.* **11**, 1322–1330 (2021).
17. Guntu, R. K., Sivaram, K. & Shetty, P. B. A holistic approach to Cr_2O_3-doped lithium lead borosilicate glasses: probing thermal stability, optical emissions, and gamma shielding. *J. Non-cryst. Solids*. **666**, 123717 (2025).
18. Yabsantia, S. et al. Enhancement of gamma and X-ray shielding behaviors in ZnO-B2O3 glasses via La2O3 addition: Experimental and theoretical investigations. *Radiat. Phys. Chem.* **237**, 112959 (2025).
19. Kaewjaeng, S. et al. Fabrication luminescence and radiation shielding properties of Gd2O3–La2O3–ZnO–B2O3–Sm2O3 glasses. *Radiat. Phys. Chem.* **202**, 110537 (2023).
20. Ebrahimi, E. & Rezvani, M. Optical and structural investigation on sodium borosilicate glasses doped with Cr2O3. *Spectrochim. Acta Part A Mol. Biomol. Spectrosc.* **190**, 534–538 (2018).
21. Sayyed, M., Abdo, M., Ali, H. E. & Sadeq, M. Impact of Y2O3 on the structural, optical, radiation shielding, and ligand field parameters of transparent borate glass containing constant CrO3 and high Na2O contents. *Ceram. Int.* **48** (14), 20485–20494 (2022).
22. Matijasevic, M. & Almazouzi, A. Effect of Cr on the mechanical properties and microstructure of Fe–Cr model alloys after n-irradiation. *J. Nucl. Mater.* **377** (1), 147–154 (2008).
23. Siwadamrongpong, S., Koide, M. & Matusita, K. Prediction of chloride solubility in CaO–Al2O3–SiO2 glass systems. *J. Non-cryst. Solids*. **347**, 1–3 (2004).
24. Chen, X., Karpukhina, N., Brauer, D. S. & Hill, R. G. High chloride content calcium silicate glasses. *Phys. Chem. Chem. Phys.* **19** (10), 7078–7085 (2017).
25. Caurant, D. & Majérus, O. Glasses and glass-ceramics for nuclear waste immobilization. *Encyclopedia materials: Tech. Ceram. glasses*. **2**, 762–789 (2021).
26. Wang, P. et al. The mechanical properties and chemical durability of granite wastes based glass-ceramics for immobilization of high-level nuclear wastes. *Ceram. Int.* **50** (13), 24907–24912 (2024).

27. Budida, J., Rao, C. S., Chand, N. R., Guntu, R. K. & Mohan, N. K. Multifunctional Pr2O3 doped lithium fluoro lanthanum oxy lead borate glasses for advanced photonic and radiation shielding applications. *J. Alloys Compd.* **1037**, 182433 (2025).
28. Madshal, M., El-Damrawi, G., Abdelghany, A. & Abdelghany, M. Structural studies and physical properties of Gd2O3-doped borate glass. *J. Mater. Sci.: Mater. Electron.* **32** (11), 14642–14653 (2021).
29. Ornketphon, O. et al. Photon shielding properties of oxyfluoride aluminophosphate glass added with Sb2O3 by using PHITS Monte Carlo simulation and experimental methods. *Radiat. Phys. Chem.* **224**, 111993 (2024).
30. Bashir, A. R., Rana, A. M., Ullah, S., Shah, S. I. W. & Wazir-ud-Din, M. Investigation of the radiation shielding and physical properties of strontium-zinc-borate glasses. *Nexus Future Mater.* **2**, 245 (2025).
31. Inaba, S., Fujino, S. & Morinaga, K. Young's modulus and compositional parameters of oxide glasses. *J. Am. Ceram. Soc.* **82** (12), 3501–3507 (1999).
32. Hildenbrand, D. Dissociation energies of the monochlorides and dichlorides of Cr, Mn, Fe, Co, and Ni. *J. Chem. Phys.* **103** (7), 2634–2641 (1995).
33. Makishima, A. & Mackenzie, J. D. Direct calculation of Young's moidulus of glass. *J. Non-cryst. Solids*. **12** (1), 35–45 (1973).
34. Makishima, A. & Mackenzie, J. D. Calculation of bulk modulus, shear modulus and Poisson's ratio of glass. *J. Non-cryst. Solids*. **17** (2), 147–157 (1975).
35. Aktas, B. et al. Effect of Er2O3 on structural, mechanical, and optical properties of Al2O3-Na2O-B2O3-SiO2 glass. *J. Non-cryst. Solids*. **584**, 121516 (2022).
36. Sayyed, M., Mahmoud, K. & Kaky, K. M. Exploring the BaO/B2O3 substitution impacts on B2O3-ZnO-PbO-BaO glasses: Comprehensive analysis for physical, optical, mechanical, and radiation shielding properties. *Ann. Nucl. Energy*. **208**, 110765 (2024).
37. Zhou, Y. C. et al. Theoretical Prediction and Experimental Investigation on the Thermal and Mechanical Properties of Bulk β-Yb 2 Si 2 O 7. *J. Am. Ceram. Soc.* **96** (12), 3891–3900 (2013).
38. Şakar, E., Özpolat, Ö. F., Alım, B., Sayyed, M. I. & Kurudirek, M. Phy-X/PSD: development of a user friendly online software for calculation of parameters relevant to radiation shielding and dosimetry. *Radiat. Phys. Chem.* **166**, 108496 (2020).
39. Buyuk, B., Keskin, O., Karabul, Y., Kocak, İ. & Kamislioglu, M. Production, analysis, and assessment of gamma-ray shielding performance of Gd2O3-Doped ZnO–B2O3 glasses using MCNP6 simulations. *Radiat. Phys. Chem.* **232**, 112671 (2025).
40. Kaewjaeng, S. et al. High transparency La2O3-CaO-B2O3-SiO2 glass for diagnosis x-rays shielding material application. *Radiat. Phys. Chem.* **160**, 41–47 (2019).
41. Ornketphon, O. et al. Fabrication of colorless phosphate glass doped with Bi2O3 for lead-free radiation shielding in X-Rayand gamma-rays medical applications: A study using PHITS Monte Carlo simulation and experimental analysis. *Radiat. Phys. Chem.* **237**, 113015 (2025).
42. Imheidat, M. A., l, S. E., Alawaideh & Preparation and investigation of the radiation protection properties of borate glasses with enhanced PbO2 and BaO content. *Nexus Future Mater.* **2**, 632780 (2025).
43. Ruiz, E. Radiation shielding analysis of barium-titanium-borate glasses doped with zinc oxide. *Nexus Future Mater.* **1**, 80–85 (2024).
44. Lincuna, J. R. S., Ueda, K. & Narushima, T. Borate bioactive glass powders: Sol–gel synthesis via metathesis reaction and evaluation of dissolution in simulated body fluid. *Ceram. Int.* **52**, 5174–5185 (2025).
45. Lincuna, J. R. S., Ueda, K. & Narushima, T. Citric acid-assisted sol–gel synthesis of highly reactive borate-based bioactive glass powders. *J. Non-cryst. Solids*. **666**, 123637 (2025).
46. Alsaif, N. A. et al. Impact of Sm3 + ions on the structure, physical, FTIR spectroscopy and mechano-radiation shielding capabilities of high dense CdO–Bi2O3–SiO2 glasses. *Appl. Phys. A*. **131** (4), 314 (2025).
47. Alsaif, N. A. et al. FTIR, Dielectric and Radiation Accumulative Factors of B2O3-NaF-ZnO-Bi2O3 Glasses Reinforced with CuO/Fe2O3. *J. Electron. Mater.* **54** (6), 4908–4917 (2025).
48. Ahmed, R. & Sallam, O. Optical properties, FTIR, and electron spin resonance analysis on the impact of gamma irradiation on fluorophosphate glasses doped with Iron (III) oxide. *Ceram. Int.* **50** (18), 31767–31779 (2024).
49. Sun, Y. et al. Effect of He ions irradiation on the leaching behavior of borosilicate glasses. *J. Am. Ceram. Soc.* **108** (5), e20370 (2025).
50. Hefnawy, A., Elkhoshkhany, N., Mahgoub, F. & Hussein, M. Mechanical properties and electrochemical behavior of borosilicate glass system. *Digest J. Nanomaterials Biostructures (DJNB)*. **16**, 2 (2021).
51. Sherer, M. A. S., Visconti, P. J., Ritenour, E. R. & Haynes, K. *Radiation protection in medical radiography* (Elsevier Health Sciences, 2013).
52. Hoheisel, M. Review of medical imaging with emphasis on X-ray detectors. *Nucl. Instrum. Methods Phys. Res., Sect. A*. **563** (1), 215–224 (2006).
53. Poirier, Y., Belley, M. D., Dewhirst, M. W., Yoshizumic, T. T. & Down, J. D. Transitioning from gamma rays to X rays for comparable biomedical research irradiations: Energy matters. *Radiat. Res.* **193** (6), 506–511 (2020).
54. Alomayrah, N. et al. Gamma attenuation properties of Tm2O3 doped tellurite glass for radiation shielding. *J. Radiation Res. Appl. Sci.* **17** (3), 100983 (2024).
55. Thulasi, P. *Studies on gamma ray inter-action parameters of selected thermoplastic, biopolymer and rare earth oxide samples* (Department of Physics, University of Calicut, 2023).
56. Budida, J., Rao, C. S., Chand, N. R. & Guntu, R. K. Spectral and Structural Tailoring of Sm2O3-Doped LiF-La2O3-PbO-B2O3 Glasses for Advanced Luminescent Devices: J. Budida et al. *J. Electron. Mater.* **54** (11), 10611–10647 (2025).
57. Zakaly, H. M. et al. Probing the elasticity and radiation protection potential of neodymium (III) doped zinc and niobium tellurite glasses: An integrated simulated and applied physics perspective. *Mater. Today Commun.* **37**, 107113 (2023).
58. Bashter, I. Calculation of radiation attenuation coefficients for shielding concretes. *Ann. Nucl. Energy*. **24** (17), 1389–1401 (1997).

Author contributions

All authors whose names appear on the submission made substantial contributions to the conception or design of the work; and analysis, of data. Material preparation, and data analysis were performed by [**Norah Alsairy and M.A. Madshal**]. Visualization is performed by [**Ashrf althbiti**]. The first draft of the manuscript was written by [**Norah Alsairy, M.A. Madshal, and Ashrf althbiti**] and all authors commented on previous versions of the manuscript. All authors read and approved the final manuscript.

Acknowledgements

The authors would like to acknowledge Deanship of Graduate Studies and Scientific Research, Taif University for funding this work.

Declarations

Competing interests
The authors declare no competing interests.

Additional information
Correspondence and requests for materials should be addressed to M.A.M.

Reprints and permissions information is available at www.nature.com/reprints.

Publisher's note Springer Nature remains neutral with regard to jurisdictional claims in published maps and institutional affiliations.